Different Martian Crustal Seismic Velocities Across the Dichotomy Boundary From Multi-Orbiting Surface Waves

Jiaqi Li, Caroline Beghein, Philippe Lognonné, Scott Mclennan, Mark Wieczorek, Mark Panning, Brigitte Knapmeyer-Endrun, Paul Davis, W. Bruce Banerdt

To cite this version:

Jiaqi Li, Caroline Beghein, Philippe Lognonné, Scott Mclennan, Mark Wieczorek, et al.. Different Martian Crustal Seismic Velocities Across the Dichotomy Boundary From Multi-Orbiting Surface Waves. Geophysical Research Letters, 2022, 50 (1), 10.1029/2022GL101243 . hal-03938829v2

HAL Id: hal-03938829
https://u-paris.hal.science/hal-03938829v2

Submitted on 20 May 2023

Geophysical Research Letters®

RESEARCH LETTER
10.1029/2022GL101243

Special Section:
The Large Marsquake of Sol 1222

Key Points:

- Analyses of the minor-arc and major-arc Rayleigh waves reveal different Martian crustal structures across the dichotomy boundary
- The average shear-wave velocity is faster in the highlands than in the lowlands near the dichotomy boundary
- The lower shear-wave velocity in the lowlands may be due to the presence of sedimentary rocks and relatively higher porosity

Supporting Information:

Supporting Information may be found in the online version of this article.

Correspondence to:
J. Li,
jli@epss.ucla.edu

Citation:
Li, J., Beghein, C., Lognonné, P., McLennan, S. M., Wieczorek, M. A., Panning, M. P., et al. (2023). Different Martian crustal seismic velocities across the dichotomy boundary from multi-orbiting surface waves. *Geophysical Research Letters*, *50*, e2022GL101243. https://doi.org/10.1029/2022GL101243

Received 29 SEP 2022
Accepted 18 NOV 2022

Author Contributions:
Conceptualization: Jiaqi Li
Data curation: Jiaqi Li, Paul Davis
Formal analysis: Jiaqi Li
Funding acquisition: Caroline Beghein
Investigation: Jiaqi Li, Philippe Lognonné, Scott M. McLennan
Methodology: Jiaqi Li, Philippe Lognonné, Mark A. Wieczorek
Resources: Jiaqi Li
Software: Jiaqi Li, Caroline Beghein

Different Martian Crustal Seismic Velocities Across the Dichotomy Boundary From Multi-Orbiting Surface Waves

Jiaqi Li[1], Caroline Beghein[1], Philippe Lognonné[2], Scott M. McLennan[3], Mark A. Wieczorek[4], Mark P. Panning[5], Brigitte Knapmeyer-Endrun[6], Paul Davis[1], and W. Bruce Banerdt[5]

[1]Department of Earth, Planetary, and Space Sciences, University of California, Los Angeles, CA, USA, [2]CNRS, Institut de physique du globe de Paris, Université Paris Cité, Paris, France, [3]Department of Geosciences, Stony Brook University, Stony Brook, NY, USA, [4]Laboratoire Lagrange, Observatoire de la Côte d'Azur, CNRS, Université Côte d'Azur, Nice, France, [5]Jet Propulsion Laboratory, California Institute of Technology, Pasadena, CA, USA, [6]Bensberg Observatory, University of Cologne, Bergisch Gladbach, Germany

Abstract

We have observed both minor-arc (R1) and major-arc (R2) Rayleigh waves for the largest marsquake (magnitude of 4.7 ± 0.2) ever recorded. Along the R1 path (in the lowlands), inversion results show that a simple, two-layer model with an interface located at 21–29 km and an upper crustal shear-wave velocity of 3.05–3.17 km/s can fit the group velocity measurements. Along the R2 path, observations can be explained by upper crustal thickness models constrained from gravity data and upper crustal shear-wave velocities of 2.61–3.27 and 3.28–3.52 km/s in the lowlands and highlands, respectively. The shear-wave velocity being faster in the highlands than in the lowlands indicates the possible existence of sedimentary rocks, and relatively higher porosity in the lowlands.

Plain Language Summary

The largest marsquake ever recorded occurred recently and waves propagating at the surface, called surface waves, have been observed. Owing to the relatively large magnitude (i.e., 4.7 ± 0.2) of this event, surface wave energy is still clearly visible after one orbit around the red planet. The shortest path taken by the wave propagating between the source and the receiver is located in the northern lowlands, near the boundary with the southern highlands (called dichotomy). The surface wave traveling in the opposite direction, following the longer distance between the quake and the seismic station, mostly passes through the highlands. Analyses of these two paths reveal that the average shear-wave velocity is faster in the highlands than in the lowlands near the dichotomy boundary. This lower velocity in the lowlands may be due to the presence of thick accumulations of sedimentary rocks and relatively higher porosity.

1. Introduction

The InSight (Banerdt et al., 2020) mission landed a very broadband seismometer (Lognonné et al., 2019), on Mars in Nov 2018 to better understand the structure, evolution, and differentiation of the Martian crust. In nearly three and a half years, more than one thousand marsquakes and several impact events have been recorded (Clinton et al., 2021; Garcia et al., 2022; Posiolova et al., 2022). So far, multiple body-wave signals have been clearly recorded (Clinton et al., 2021), but observable surface-wave signals were only recently reported for two impact events (Kim et al., 2022).

Due to the lack of surface wave observations, previous seismological studies of the Martian crust and the topmost mantle were mainly based on body waves and ambient noise correlations (e.g., Compaire et al., 2021; Knapmeyer-Endrun et al., 2021; Li, Beghein, Davis, et al., 2022; Li, Beghein, Wookey, et al., 2022; Lognonné et al., 2020; Schimmel et al., 2021). Since the ray paths of the above-mentioned signals are nearly vertically incident beneath the seismometer, most of the sampled sub-surface structures are limited to the vicinity of the InSight landing site (i.e., within a radius of ~50 km). Nevertheless, there were attempts to constrain the crustal structures at other locations (e.g., Li, Beghein, McLennan, et al., 2022).

On the 1222nd Martian day (sol) of the InSight mission, the largest marsquake (S1222a) ever recorded occurred with a magnitude of 4.7 ± 0.2, which corresponds to energy five times greater than the second-largest event (InSight Marsquake Service, 2022; Kawamura et al., 2022). For the first time, both Rayleigh and Love waves were observed on a planet other than Earth (Beghein et al., 2022; Kawamura et al., 2022; Xu et al., 2022).

Supervision: Caroline Beghein
Validation: Caroline Beghein, Philippe Lognonné, Scott M. McLennan, Mark A. Wieczorek, Mark P. Panning, Brigitte Knapmeyer-Endrun, W. Bruce Banerdt
Visualization: Jiaqi Li
Writing – original draft: Jiaqi Li, Caroline Beghein, Scott M. McLennan
Writing – review & editing: Jiaqi Li, Caroline Beghein, Philippe Lognonné, Scott M. McLennan, Brigitte Knapmeyer-Endrun

On a radially stratified, laterally homogeneous sphere, a surface wave travels along the great-circle path. The wave that travels along the shorter path between the source and the receiver is named the minor-arc Rayleigh wave (R1). The wave that travels in the other direction, along the longer path, is named the major-arc Rayleigh wave (R2). The Rayleigh wave arrival is called R3 when the minor-arc wave circuits the globe and eventually reaches the station again. On Earth, R2 and R3 can fill the gap of poorly covered areas in tomographic models (constrained by R1 alone) and thus enhance the resolution (e.g., Trampert & Woodhouse, 1996). On Mars, the R2 and R3 observations are very important since there is only one station and thus there are lots of gaps to cover.

To observe the R2 and R3 Rayleigh waves, which are of much smaller amplitude than R1, the minimum moment magnitude was estimated to be M_w 6.0 for quiet stations on Earth (Panning et al., 2015). On Mars, the minimum requirement for marsquakes is between M_w 4.6 and M_w 5.3, mainly due to Mars's smaller radius (Panning et al., 2015). As predicted, the large magnitude of event S1222a enabled observations of R2 and R3 on Mars (Panning et al., 2023).

The epicentral distance of event S1222a is 37.0° ± 1.6°, and the back azimuth is estimated to be between 96° and 112° (Kawamura et al., 2022), placing the location of S1222a in the lowlands and near the dichotomy boundary. The dichotomy boundary separates the northern lowlands and southern highlands and has highly debated origins (Andrews-Hanna et al., 2008; Frey, 2006; Marinova et al., 2008; Zhong & Zuber, 2001). The R2 and R3 Rayleigh waves pass through both the lowlands and the highlands (Figure 1), which are far from the InSight lander and were scarcely sampled by seismic waves with the previously recorded marsquakes. These observations allow us to put new constraints on the crustal structure away from the lander in both the lowlands and the highlands.

In this paper, we first measured the group velocity of the Rayleigh waves along the R1, R2, and R3 paths. Then, we performed inversions for R1 and R2 (the R3 measurements are less reliable, as explained below) to derive seismic velocity models that could explain the observations. After comparing the seismic velocity profiles in the lowlands and highlands, we discuss the possible effects of the crustal variations on the observed group velocities of the minor- and major-arc Rayleigh waves.

2. Data

The minor-arc Rayleigh wave, which travels 2,193 ± 95 km (using an equatorial radius of 3,396.2 km), arrives around 800 s after the origin time on the seismogram and can be observed over a relatively broad frequency band on both the vertical (i.e., 10–60 s, in Figure 2a) and the radial components (Figure S1 in Supporting Information S1). Since the seismometer is in an extremely harsh environment, the diurnal temperature variations could generate one-sided pulses (hereafter referred to as glitches) that can contaminate the seismic signals. A comparison between the raw data and the deglitched data (Scholz et al., 2020) shows that there is no significant glitch near the R1 arrival time (Figure S1 in Supporting Information S1).

R2 travels a much longer distance of about 19,146 ∓ 95 km and arrives around 6,650 s after the origin time (Figure 2b). R2 is observed within a relatively narrow frequency range (i.e., 25–35 s), and the amplitude is only about one-fourth of that of R1. Although there is no glitch near the R2 arrival, another signal of a slightly smaller amplitude occurs at about 6,800 to 7,000 s. Panning et al. (2023) excluded this signal as being the R2 phase since this later arrival does not show strong and consistent elliptical particle motions at different frequency bands (which is expected for the Rayleigh wave), and the corresponding marsquake location would be highly inconsistent with the one constrained by body waves (Kawamura et al., 2022). Therefore, we prefer selecting the R2 signal at around 6,650 s.

The R3 wave, which travels 23,532 ± 95 km, overlaps with a glitch in the raw data (Figure 2b). R3 is still visible on the deglitched data and exhibits arrival times of about 8,100 s. However, since the deglitching procedure may not perfectly fit the real glitch and thus could also remove some seismic signals, the R3 signals (e.g., the arrival time and amplitude) are less reliable than R1 or R2. Therefore, in the following analysis, we mainly focus on R1 and R2 and consider R3 as auxiliary data for benchmarking purposes.

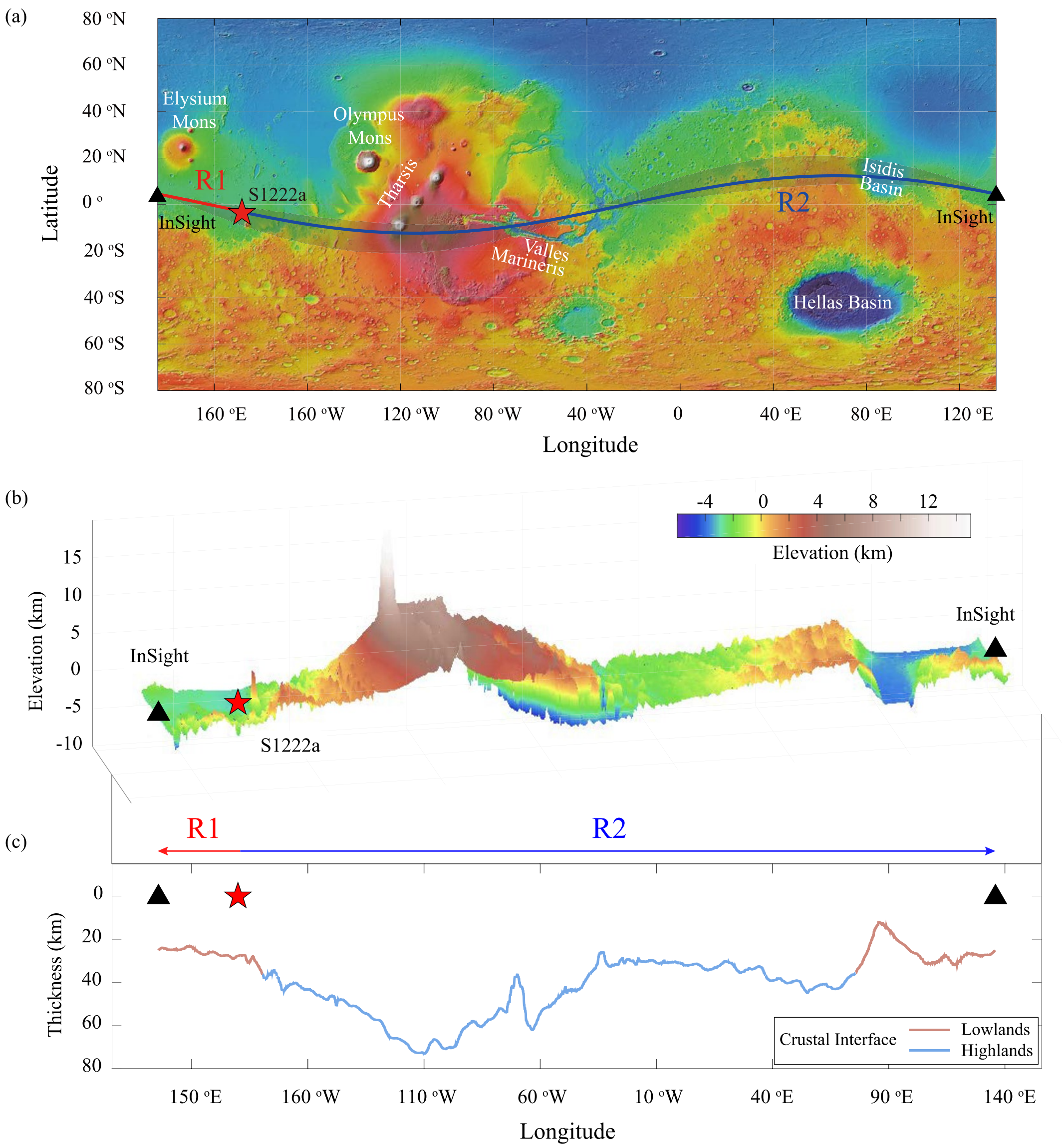

Figure 1. (a) Mars Orbiter Laser Altimeter (Smith et al., 2001) map. The red star marks the optimal hypocenter of event S1222a (Kawamura et al., 2022), and the black triangle indicates the broadband seismometer of the InSight mission. The red and blue curves denote the great-circle paths of R1 and R2, respectively. The shaded gray areas illustrate all possible paths for R1 and R2 based on the back azimuth uncertainty of the event location (Kawamura et al., 2022). (b) Elevation variations along the Rayleigh wave paths shown in (a). Regions within 10° of the optimal great-circle path are displayed to account for the finite frequency effect (e.g., Zhou et al., 2004). (c) Lateral variations of the upper crust along the Rayleigh wave great-circle path in (a). The depth of the interface at the InSight lander site is fixed at 26 km from the R1 inversion (in Figure 3c), and the relative variations are constrained by gravity data (Wieczorek et al., 2022). The location of the dichotomy boundary is from Tanaka et al. (2014).

3. Method and Results

3.1. Group Velocity Measurements

To measure the Rayleigh wave group velocity, we first performed a multiple filter analysis (Herrmann, 2013) to calculate the energy of the waveform envelope at different periods (Figures 2c and 2d). Then, we selected the optimal group velocity at each period corresponding to the maximum energy (in dB) of the waveform envelope. Finally, we defined the uncertainty of the measurements using a 1 dB threshold (Beghein et al., 2010), that is, group velocities with amplitudes within 1 dB of the maximum amplitude are viewed as acceptable measurements.

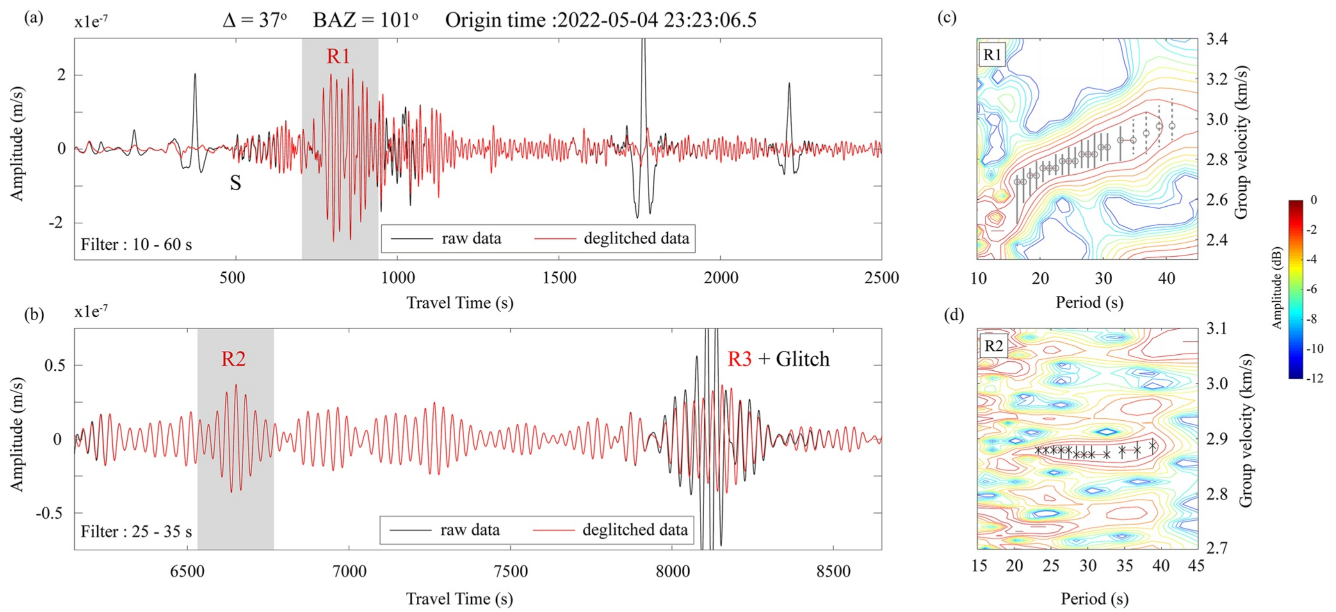

Figure 2. (a) Seismic waveforms (after removing the instrument response and bandpass filter from 10 to 60 s) on the vertical component near the arrival times of the S wave and R1. The black and red waveforms are the velocity records from the raw data set and deglitched data set, respectively. The shaded gray region marks the time window in which we performed the multiple filter analysis in (c). (b) Waveforms on the vertical component near the arrivals of R2 and R3 with a filter band of 25–35 s. (c) Multiple filter analysis (Herrmann, 2013) for R1 on the vertical component. The *x*- and *y*-axes are the period and group velocity, respectively. Color scales represent the energy contours (in dB) of the waveform envelope. The black circles indicate the preferred group velocity measurements. The vertical gray error bar spans 1 dB. Note that at periods greater than 32 s, the R1 measurements show discrepancies between the vertical and radial components (see Figure S2 in Supporting Information S1) and thus are less reliable (denoted by the dashed error bars). (d) Similar to (c) but for R2 on the vertical component.

The reliable period range for the R1 signal on the vertical component is from 17 to 32 s, where the group velocities are consistent with those measured on the radial component (Figure S2 in Supporting Information S1). For the average group velocity along the R1 path, there are clear signs of positive dispersion, that is, the group velocity increases with the period. Given the origin time of 4 May 2022 23:23:06.5 (UTC) and the epicentral distance of 37° (Kawamura et al., 2022), the R1 group velocity increases from 2.70 ± 0.05 km/s at 17 s to 2.95 ± 0.05 km/s at 41 s (Figure 2c, see Text S1 in Supporting Information S1 for discussions on the location error).

We applied the same analysis to the R2 signal and found that it exhibits little dispersion between periods of 23 and 39 s, with a nearly constant group velocity of 2.90 ± 0.01 km/s (Figure 2d). It is worth mentioning that the uncertainty of the R2 group velocity is much smaller (less than one-fifth) than that of R1 due to its longer travel time (See Text S1 in Supporting Information S1 for details).

Figure 2b shows that R3 is significantly affected by a glitch. Nevertheless, based on the deglitched data, the multiple filter analysis shows little dispersion and a nearly constant group velocity of about 2.90 ± 0.02 km/s (Figure S3 in Supporting Information S1). This similar values for R2 and R3 group velocities confirm the reliability of the R2 measurements given their similar paths (i.e., they share the same path for about 19,000 km or about 80% of the R3 path length).

3.2. Inversion Along the R1 Path

We inverted the group velocity measurements to constrain the average seismic velocity profile along the R1 path. Specifically, we used a Niche Genetic Algorithm (Koper et al., 1999; Li et al., 2021) to sample different possible models and the CPS code package (Herrmann, 2013) to calculate the group velocities predicted by these models at different periods.

We chose to represent the model with a layered crustal parameterization because previous receiver function studies (Kim et al., 2021; Knapmeyer-Endrun et al., 2021; Lognonné et al., 2020) exhibited the presence of sharp interfaces in the crust. In addition, we preferred to set the number of layers to two because this model setting with only three free parameters (i.e., the depth of the interface, and the shear-wave velocities above and below this

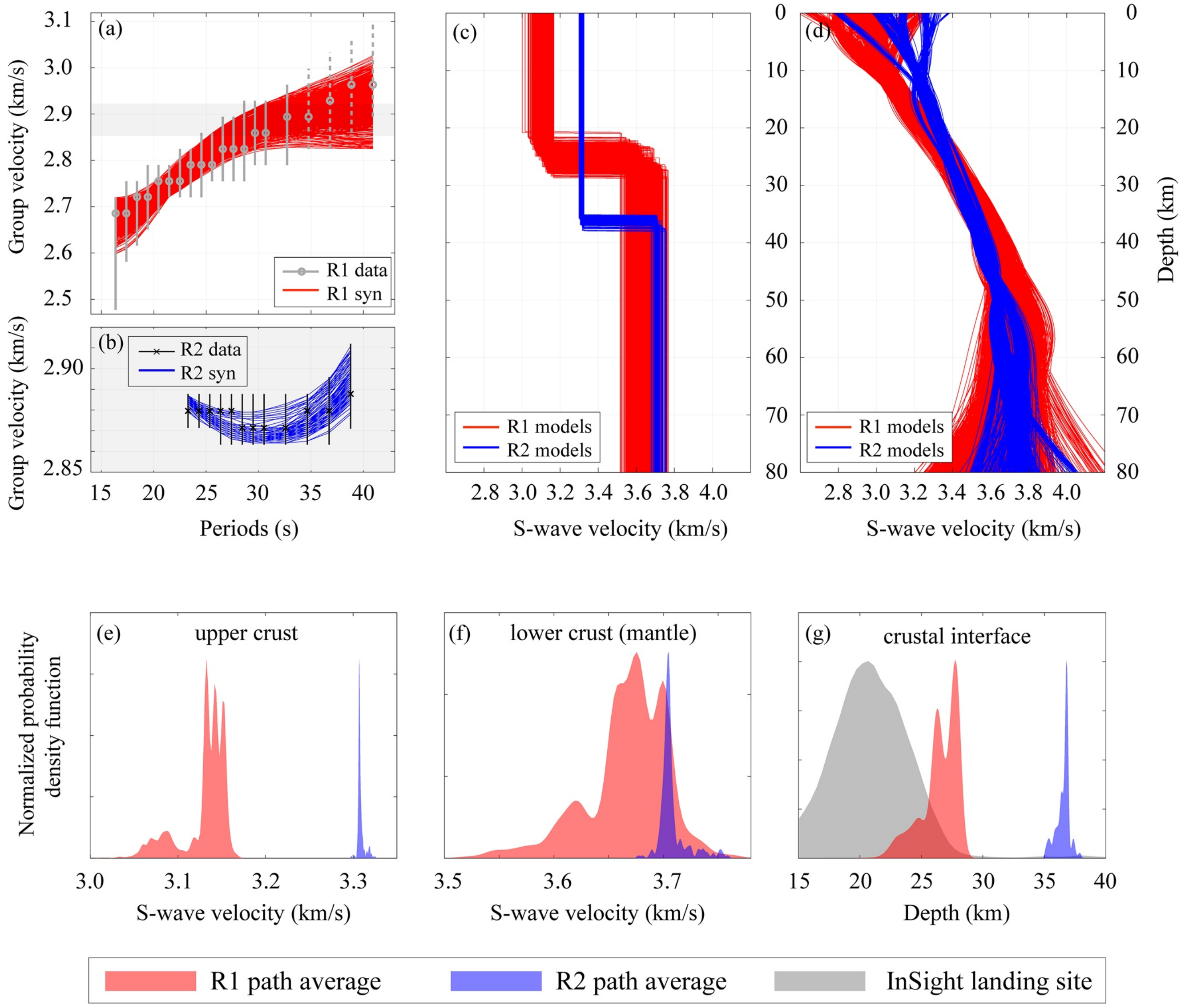

Figure 3. (a) Group velocity measurements (gray circles), uncertainties (vertical bars), and synthetic group velocity dispersion curves (in red, corresponding to the models shown in (c) with the same color) along the R1 path. The range of the *y*-axis (i.e., group velocity) in the shaded gray region is the same as that in (b). (b) Similar to (a), but for the R2 path, and the corresponding models (in blue) shown in (c). (c) Shear-wave velocity profiles for all the acceptable models along the R1 (in red) and R2 (in blue) paths from the inversion for the discontinuity model setting. (d) Similar to (c), but for the smoothed (i.e., third-order B-splines) model setting. (e) Normalized probability density functions of the shear-wave velocities in the upper crust for all the acceptable models (R1 models in red, and R2 models in blue) in (c). (f) Similar to (e), but for the shear-wave velocities in the lower crust and mantle (i.e., down to 80 km). (g) Similar to (e), but for the depth of the crustal interface. The probability density function in gray shows the depth of the intra-crustal discontinuity beneath the landing site from the receiver function study (Knapmeyer-Endrun et al., 2021).

interface) is less likely prone to overfitting the data. If this simplified model fails to fit the observed group velocities, we can then consider a more complex model. Based on the sensitivity curves of the Rayleigh waves at periods shorter than 40 s (Figure S4 in Supporting Information S1), we only constrained the structure above 80 km depth. At greater depths, we used the values of the InSight_KKS21GP model (Khan et al., 2021; Knapmeyer-Endrun et al., 2021; Stähler et al., 2021a, 2021b), which was constructed from teleseismic body waves (See Text S2 for the model setup). We also tested a smoothed model setting with eight third-order B-splines (Figure 3d) and found that the average velocities above (or below) the interface are similar between the discontinuity and the smoothed model settings (Figure S5 in Supporting Information S1).

Figure 3c shows that a simplified model with two layers in the top 80 km can reproduce the R1 dispersion curve. Specifically, the shear-wave velocity is estimated to be 3.05–3.17 km/s in the top layer, and 3.50–3.80 km/s in the bottom layer. The interface depth estimation is 21–29 km. Figure 3g shows that the depth of the inverted interface along the R1 path overlaps with the depth of the intra-crustal interface beneath the InSight lander constrained by the receiver function (Knapmeyer-Endrun et al., 2021), although the mean value deviates (possibly due to the differences in the regions to which those two methods are sensitive).

We note that Knapmeyer-Endrun et al. (2021) provided two possible crustal thicknesses beneath the lander: a thinner crustal model with a shallow Moho depth of 20 ± 5 km, and a thicker crustal model (where the interface at around 20 km is interpreted as an intra-crustal interface) with a deeper Moho depth of 39 ± 8 km (though with a smaller impedance contrast across this deeper Moho). Here, we prefer to refer to the interface at 21–29 km (inferred in this study) as the intra-crustal interface since subsequent studies from Kim et al. (2021) and Durán et al. (2022) favored the thicker crustal scenario. We also want to note that we cannot resolve the deeper Moho (if it exists) since only the discontinuity with the most significant velocity jump will be detected with the current one-interface setting.

3.3. Inversion Along the R2 Path

We note that it is reasonable to perform the inversion with a representative one-interface model along the entirety of the R1 path since there are few topographic changes (e.g., Figure 4a). However, along the R2 path, it may be preferable to account for the significant lateral variations in both topography and crustal thickness (Wieczorek et al., 2022), rather than simply using an average one-interface model (e.g., Figure 3c) to explain the R2 dispersion curve in Figure 3b.

We thus divided the R2 path into 3,230 sub-paths, and within each sub-path (of which the length is shorter than the wavelength) we can assume a one-interface model with a similar setup as for R1. The upper crustal thickness models along the R2 path are modified from Wieczorek et al. (2022) as prior information (See Text S3 in Supporting Information for the R2 model setup). There are only three free parameters in the R2 inversion, that is, the upper crustal shear-wave velocities in the lowlands (V_L) and highlands (V_H), and the shear-wave velocity below the crustal interface (V_2).

Grid search results show that within the given range of V_2 (i.e., 3.50–3.80 km/s from the R1 inversion results in Figure 3e), a series of models (Figure 4b), with upper crustal velocities of 2.61–3.27 km/s in the lowlands and 3.28–3.52 km/s in the highlands, can fit the R2 measurements (Figure S6 in Supporting Information S1).

The probability density functions in Figure 4c illustrate that the upper crustal shear-wave velocity in the highlands (i.e., 3.28–3.52 km/s) is systematically faster than that in the lowlands (i.e., 2.61–3.27 km/s). We further reduced the number of acceptable models from the R2 inversion with the extra constraint from the R1 inversion (i.e., upper crustal velocity in the lowlands should be in the range of 3.05–3.17 km/s). The down-selected models, which satisfy both the R1 and R2 observations, also demonstrate a greater upper crustal shear-wave velocity in the highlands (i.e., 3.27–3.33 km/s) than that in the lowlands (i.e., 3.05–3.17 km/s).

4. Discussion

4.1. Comparison With the InSight Landing Site

The most sensitive depth range of the Rayleigh waves analyzed is from ~10 to 50 km (Figure S7 in Supporting Information S1), though there are also a few sensitivities to greater depths. Therefore, we have better constraints on the upper crust (i.e., above the crustal interface), than the lower crust and mantle.

Since Lognonné et al. (2020) and Knapmeyer-Endrun et al. (2021) obtained the first Martian crustal structure beneath the InSight landing site, whether it represents local geologies or global features has been debated. In the similar depth range of ~8–20 km, beneath the lander, the S-wave velocity is estimated to be 2.2 ± 0.6 km/s (Knapmeyer-Endrun et al., 2021). This upper crustal velocity beneath the lander (also located in the lowlands) is significantly smaller than the average velocity (i.e., ~3 km/s, see Figures 4c and 4d) along the surface wave path in the lowlands.

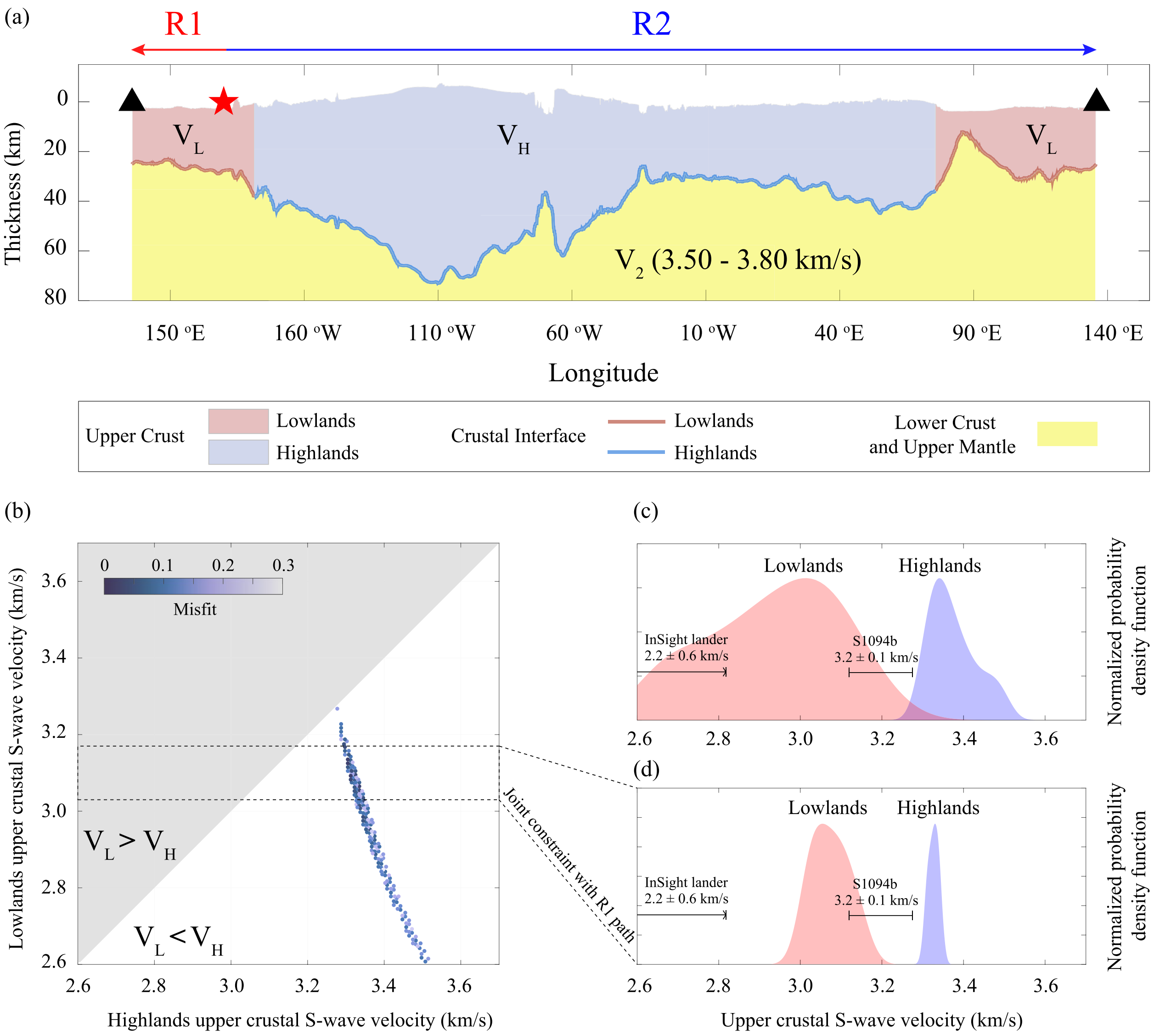

Figure 4. (a) Model setup for the R2 inversion. The upper crustal thickness models modified from Wieczorek et al. (2022) are used as prior information and fixed in the inversion. Along the R2 path, the only three free parameters are the upper crustal shear-wave velocities in the lowlands (V_L) and highlands (V_H), and the shear-wave velocity (V_2) below the crustal interface (See Text S3 in Supporting Information S1 for the R2 model setup). (b) Grid search results for the upper crustal shear-wave velocity in the lowlands (V_L, the y-axis), and in the highlands (V_H, the x-axis) along the R2 path. The acceptable models that can fit the R2 measurements are shown as filled circles, with color scales corresponding to the misfits (See Text S2 in Supporting Information S1 for the misfit function). The dashed region indicates where the models also satisfy the R1 observations (i.e., an upper crustal shear-wave velocity of 3.05–3.17 km/s in the lowlands). The shaded gray area to the left of the diagonal indicates the region where the upper crustal velocity in the lowlands is faster than that in the highlands. Note that at each grid point, a grid search for the shear-wave velocity below the crustal interface (V_2) is also performed. (c) Normalized probability functions of the upper crustal shear-wave velocities (lowlands models are in red, and highlands models are in blue) for the acceptable models in (b). S-wave velocities beneath the InSight lander (in the depth range of ∼8–20 km, Knapmeyer-Endrun et al., 2021) and along the great circle path from the meteorite impact S1094b (Kim et al., 2022) are also annotated. (d) Similar to (c), but for the models that satisfy both the R1 and R2 observations (i.e., in the dashed region in (b)).

Similar S-wave velocity (i.e., ∼3.2 km/s) of the upper crust in the lowlands (along the surface wave path from a meteorite impact) has also been recently reported (Kim et al., 2022). This faster velocity has been attributed to the different compositions and/or reduced porosity in the volcanic areas along the path (Kim et al., 2022).

For marsquake S1222a, the surface wave path also likely traverses the volcanic units in the lowlands (Figure S8 in Supporting Information S1). Therefore, the crustal porosity may have been occluded or obscured by later magmatism (e.g., Wilson & Head, 1994), resulting in a faster S-wave velocity than beneath the landing site (where there are higher porosities).

4.2. Upper Crust in the Lowlands and the Highlands

The upper crust velocity in the lowlands, though larger than the InSight landing site, is systematically smaller than that in the highlands (Figures 4c and 4d). Possible interpretations for the smaller upper crustal shear-wave velocity values in the lowlands than in the highlands could include some combination of differing compositions, reductions in porosity at depth, and/or the presence of sedimentary rocks.

Variations in lithology and rock compositions are a common major cause of regional variations in crustal seismic structure (Rudnick & Fountain, 1995). The Martian crust is thought to be of basaltic composition on average (Taylor & McLennan, 2009). Recently, using global crustal thickness and thermal evolution models, Thiriet et al. (2018) suggested that felsic rocks were more common in the Noachian-dominated southern highlands, leading to an average bulk density of 480 kg/m^3 less than the northern lowland crust. However, this density difference should lead to lower, rather than higher, seismic velocities (for a wide range of lithologies, e.g., Brocher, 2005) in the highlands.

Compositional differences could also affect the thermal regime and thus have an indirect influence on seismic velocities. For example, a more differentiated southern highland crust would also be characterized by higher abundances of heat-producing elements (Thiriet et al., 2018; Wieczorek et al., 2022) and, when coupled with a thicker crust, higher heat flow (e.g., Hahn et al., 2011; Parro et al., 2017). A distinctive crustal thermal regime could lead to very different depth-dependent porosity behavior.

Porosity can also significantly affect the seismic wave speed such that higher porosity results in lower shear-wave velocity (e.g., Manga & Wright, 2021). Both compaction and viscous deformation will result in porosity reduction with depth. Gyalay et al. (2020) showed that the closure of pore space should occur over a narrow depth range of a few kilometers and all porosity should have been removed for depths greater than about 12–23 km (Wieczorek et al., 2022). Accordingly, in the highlands, where the upper crust is thicker on average (Figure 4a) and surface heat flow is greater (Hahn et al., 2011; Parro et al., 2017), a larger proportion of the upper crust may lie beneath depths where porosity has been lost, leading to shear-wave velocities that are higher than in the northern lowlands when averaged over the thickness of the upper crust interrogated by the R2 paths.

To quantitatively assess the influence of porosity, we assumed that the velocity difference between the lowlands and highlands is affected by porosity alone. With a pore closure depth of 23 km (Wieczorek et al., 2022) and an aspect ratio of 0.1 (Heap, 2019), the velocity difference can be explained by a porosity reduction of 8%–15% (see Figure S9 and Text S4 in Supporting Information S1 for details).

The presence of thick accumulations of sedimentary rocks could also lead to lower density (and thus, for a wide range of lithologies, low shear-wave velocities, e.g., Brocher, 2005) due to a variety of features/processes, including the presence of elevated primary porosity for poorly consolidated and/or weakly cemented sedimentary rocks; secondary porosity for diagenetically altered sedimentary rocks; low-density hydrated alteration phases, such as phyllosilicates and amorphous silica, formed during chemical weathering and/or diagenesis (McLennan & Grotzinger, 2008; McLennan et al., 2019). However, for most locations on Mars, sedimentary rock thicknesses are on the order of a few kilometers at most (e.g., Bradley et al., 2002; Grotzinger & Milliken, 2012; Grotzinger et al., 2015). Therefore, based on our current knowledge of the total sedimentary mass and its distribution on Mars (e.g., Grotzinger & Milliken, 2012; McLennan, 2012), the presence of sedimentary rocks alone probably cannot explain the lower upper crustal shear-wave velocity in the lowlands, where the crustal interface is located at ∼26 km.

4.3. R2 Group Velocity

Another major difference between the group velocity along R1 and R2 is that there is positive dispersion along R1 but there is almost no dispersion along R2. We found that for a typical velocity model derived for the highlands, where the upper crustal thickness is greater than in the lowlands, the group velocity exhibits negative dispersion. Therefore, the negative dispersion in the highlands (Figure S7e in Supporting Information S1) could cancel out the positive dispersion in the lowlands (Figure S7d in Supporting Information S1), yielding little dispersion along the R2 path.

However, it is worth noting that long-period pressure-induced signals are also present in seismic data (Kenda et al., 2020; Stutzmann et al., 2021) and are carried by the environmental wind, resulting in an apparent burst of noise without dispersion. Given the relatively low signal-to-noise ratio for R2 and R3, this absence of dispersion could also be an artifact of the wind noise.

5. Conclusion

We have observed two minor-arcs (R1, and R3) and one major-arc (R2) Rayleigh waves generated by the largest marsquake ever recorded. The group velocities along the R1 path increase from 2.70 ± 0.05 km/s to 2.95 ± 0.05 km/s between periods of 17 and 42 s and can be explained by a two-layer model with a crustal interface depth of 21–29 km and an upper crustal shear-wave velocity of 3.05–3.17 km/s in the lowlands. The group velocity along the R2 path exhibits a nearly constant value of 2.90 km/s and can be explained by upper crustal thickness models constrained from gravity data and upper crustal shear-wave velocities of 2.61–3.27 km/s and 3.28–3.52 km/s in the lowlands and highlands, respectively. The lower shear-wave velocity in the lowlands compared to that in the highlands may be due to the presence of thick accumulations of sedimentary rocks, and relatively higher porosity.

Conflict of Interest

The authors declare no conflicts of interest relevant to this study.

Data Availability Statement

The data sets used in this study are achieved and released by InSight Mars SEIS Data Service and are available to the science community (InSight Mars SEIS Data Service, 2019; InSight Marsquake Service, 2022). Data sets (both the raw data and the deglitched data in SAC format, after removing the instrument response) for this research are available on the Zenodo repository: https://doi.org/10.5281/zenodo.7325555 (Li, Beghein, et al., 2022). The InSight_KKS21GP model is available on the IPGP Data Center (https://doi.org/10.18715/IPGP.2021.kpmqrnz8).

Acknowledgments
J.L. and C.B. were supported by NASA InSight PSP Grant 80NSSC18K1679 and S.M.M. by NASA InSight PSP Grant 80NSSC18K1622. M.P.P. and W.B.B. were supported by the InSight Project at the Jet Propulsion Laboratory, California Institute of Technology under a contract with the National Aeronautics and Space Administration (80NM0018D0004). P.L. and M.A.W. are supported by Agence Nationale de la Recherche (MAGIS, ANR-19-CE31-0008-08; IdEx Université Paris Cité, ANR-18-IDEX-0001) and by CNES for SEIS science support. This is InSight Contribution Number 278. InSight seismic data presented here (http://dx.doi.org/10.18715/SEIS.INSIGHT.XB_2016) are publicly available through the Planetary Data System (PDS) Geosciences node (InSight SEIS Data Bundle, 2021), the Incorporated Research Institutions for Seismology (IRIS) Data Management Center under network code XB and through the Data center of Institut de Physique du Globe, Paris. We acknowledge NASA, CNES, their partner agencies and Institutions (UKSA, SSO, DLR, JPL, IPGP-CNRS, ETHZ, IC, MPS-MPG), and the flight operations team at JPL, SISMOC, MSDS, IRIS-DMC, and PDS for providing SEED SEIS data.

References

Andrews-Hanna, J. C., Zuber, M. T., & Banerdt, W. B. (2008). The Borealis basin and the origin of the Martian crustal dichotomy. *Nature*, *453*(7199), 1212–1215. https://doi.org/10.1038/nature07011

Banerdt, W. B., Smrekar, S. E., Banfield, D., Giardini, D., Golombek, M., Johnson, C. L., et al. (2020). Initial results from the InSight mission on Mars. *Nature Geoscience*, *13*(3), 183–189. https://doi.org/10.1038/s41561-020-0544-y

Beghein, C., Arthur Snoke, J., & Fouch, M. J. (2010). Depth constraints on azimuthal anisotropy in the Great Basin from Rayleigh-wave phase velocity maps. *Earth and Planetary Science Letters*, *289*(3–4), 467–478. https://doi.org/10.1016/j.epsl.2009.11.036

Beghein, C., Li, J., Weidner, E., Maguire, R., Wookey, J., Lekić, V., et al. (2022). Crustal anisotropy in the Martian lowlands from surface waves. *Geophysical Research Letters*, *49*, e2022GL101508. https://doi.org/10.1029/2022GL101508

Bradley, B. A., Sakimoto, S. E., Frey, H., & Zimbelman, J. R. (2002). Medusae Fossae formation: New perspectives from Mars global surveyor. *Journal of Geophysical Research*, *107*(E8), E85050. https://doi.org/10.1029/2001JE001537

Brocher, T. M. (2005). Empirical relations between elastic wavespeeds and density in the Earth's crust. *Bulletin of the Seismological Society of America*, *95*(6), 2081–2092. https://doi.org/10.1785/0120050077

Clinton, J. F., Ceylan, S., van Driel, M., Giardini, D., Stähler, S. C., Böse, M., et al. (2021). The Marsquake catalogue from InSight, sols 0–478. *Physics of the Earth and Planetary Interiors*, *310*, 106595. https://doi.org/10.1016/j.pepi.2020.106595

Compaire, N., Margerin, L., Garcia, R. F., Pinot, B., Calvet, M., Orhand-Mainsant, G., et al. (2021). Autocorrelation of the ground vibrations recorded by the seis-insight seismometer on Mars. *Journal of Geophysical Research: Planets*, *126*(4), e2020JE006498. https://doi.org/10.1029/2020je006498

Durán, C., Khan, A., Ceylan, S., Zenhäusern, G., Stähler, S., Clinton, J. F., & Giardini, D. (2022). Seismology on Mars: An analysis of direct, reflected, and converted seismic body waves with implications for interior structure. *Physics of the Earth and Planetary Interiors*, *325*, 106851. https://doi.org/10.1016/j.pepi.2022.106851

Frey, H. V. (2006). Impact constraints on the age and origin of the lowlands of Mars. *Geophysical Research Letters*, *33*(8), L08S02. https://doi.org/10.1029/2005gl024484

Garcia, R. F., Daubar, I. J., Beucler, E., Posiolova, L. V., Collins, G. S., Lognonne, P., et al. (2022). Newly formed craters on Mars located using seismic and acoustic wave data from InSight. *Nature Geoscience*, *15*(10), 1–7. https://doi.org/10.1038/s41561-022-01014-0

Grotzinger, J. P., Gupta, S., Malin, M. C., Rubin, D. M., Schieber, J., Siebach, K., et al. (2015). Deposition, exhumation, and paleoclimate of an ancient lake deposit, Gale Crater, Mars. *Science*, *350*(6257), aac7575. https://doi.org/10.1126/science.aac7575

Grotzinger, J. P., & Milliken, R. E. (2012). The sedimentary rock record of Mars: Distribution, origins, and global stratigraphy. In J. P. Grotzinger & R. E. Milliken (Eds.), *Mars sedimentology* (Vol. 102, pp. 1–48). SEPM Special Publication.

Gyalay, S., Nimmo, F., Plesa, A.-C., & Wieczorek, M. (2020). Constraints on thermal history of Mars from depth of pore closure below InSight. *Geophysical Research Letters*, *47*(16), e2020Gl088653. https://doi.org/10.1029/2020gl088653

Hahn, B. C., McLennan, S. M., & Klein, E. C. (2011). Martian surface heat production and crustal heat flow from Mars Odyssey Gamma-Ray spectrometry. *Geophysical Research Letters*, *38*, 14. https://doi.org/10.1029/2011gl047435

Heap, M. J. (2019). P-and S-wave velocity of dry, water-saturated, and frozen basalt: Implications for the interpretation of Martian seismic data. *Icarus*, *330*, 11–15. https://doi.org/10.1016/j.icarus.2019.04.020

Herrmann, R. B. (2013). Computer programs in seismology: An evolving tool for instruction and research. *Seismological Research Letters*, *84*(6), 1081–1088. https://doi.org/10.1785/0220110096

InSight Marsquake Service. (2022). *Mars seismic catalogue, InSight Mission; V12 2022-10-01*. ETHZ, IPGP, JPL, ICL, University of Bristol. https://doi.org/10.12686/a18

InSight Mars SEIS Data Service. (2019). SEIS raw data, Insight Mission. IPGP, JPL, CNES, ETHZ, ICL, MPS, ISAE-Supaero, LPG, MFSC. https://doi.org/10.18715/SEIS.INSIGHT.XB_2016

InSight SEIS Data Bundle. (2021). PDS geosciences (GEO) node.

Kawamura, T., Clinton, J. F., Zenhäusern, G., Ceylan, S., Horleston, A. C., Dahmen, N. L., et al. (2022). S1222a—The largest marsquake detected by InSight. *Geophysical Research Letters*, *49*, e2022GL101543. https://doi.org/10.1029/2022GL101543

Kenda, B., Drilleau, M., Garcia, R. F., Kawamura, T., Murdoch, N., Compaire, N., et al. (2020). Subsurface structure at the InSight landing site from compliance measurements by seismic and meteorological experiments. *Journal of Geophysical Research: Planets*, *125*(6), e2020JE006387. https://doi.org/10.1029/2020je006387

Khan, A., Ceylan, S., van Driel, M., Giardini, D., Lognonné, P., Samuel, H., et al. (2021). Upper mantle structure of Mars from InSight seismic data. *Science*, *373*(6553), 434–438. https://doi.org/10.1126/science.abf2966

Kim, D., Banerdt, W. B., Ceylan, S., Giardini, D., Lekić, V., Lognonné, P., et al. (2022). Surface waves and crustal structure on Mars. *Science*, *378*(6618), 417–421. https://doi.org/10.1126/science.abq7157

Kim, D., Lekić, V., Irving, J. C., Schmerr, N., Knapmeyer-Endrun, B., Joshi, R., et al. (2021). Improving constraints on planetary interiors with PPS receiver functions. *Journal of Geophysical Research: Planets*, *126*(11), e2021JE006983. https://doi.org/10.1029/2021je006983

Knapmeyer-Endrun, B., Panning, M. P., Bissig, F., Joshi, R., Khan, A., Kim, D., et al. (2021). Thickness and structure of the martian crust from InSight seismic data. *Science*, *373*(6553), 438–443. https://doi.org/10.1126/science.abf8966

Koper, K. D., Wysession, M. E., & Wiens, D. A. (1999). Multimodal function optimization with a niching genetic algorithm: A seismological example. *Bulletin of the Seismological Society of America*, *89*(4), 978–988. https://doi.org/10.1785/bssa0890040978

Li, J., Beghein, C., Davis, P., Wieczorek, M. A., McLennan, S. M., Kim, D., et al. (2022). Crustal structure constraints from the detection of the SsPp phase on Mars. *Earth and Space Science*, e2022EA002416. https://doi.org/10.1029/2022ea002416

Li, J., Beghein, C., et al. (2022). Data for "different martian crustal seismic velocities across the dichotomy boundary from multi-orbiting surface waves". *Zenodo*. https://doi.org/10.5281/zenodo.7325555

Li, J., Beghein, C., McLennan, S., Horleston, A., Huang, Q., Bozdag, E., et al. (2022). Second seismic anchor point of the martian crustal structure away from the InSight landing site. *Nature Communications*. (preprint). https://doi.org/10.21203/rs.3.rs-1829147/v1

Li, J., Beghein, C., Wookey, J., Davis, P., Lognonné, P., Schimmel, M., et al. (2022). Evidence for crustal seismic anisotropy at the InSight lander site. *Earth and Planetary Science Letters*, *593*, 117654. https://doi.org/10.1016/j.epsl.2022.117654

Li, J., Chen, M., Koper, K. D., Zhou, T., Xi, Z., Li, S., & Li, G. (2021). FastTrip: A Fast MPI-accelerated 1D triplication waveform inversion package for constraining mantle transition zone discontinuities. *Seismological Research Letters*, *92*(4), 2647–2656. https://doi.org/10.1785/0220200475

Lognonné, P., Banerdt, W., Pike, W., Giardini, D., Christensen, U., Garcia, R. F., et al. (2020). Constraints on the shallow elastic and anelastic structure of Mars from InSight seismic data. *Nature Geoscience*, *13*(3), 213–220. https://doi.org/10.1038/s41561-020-0536-y

Lognonné, P., Banerdt, W. B., Giardini, D., Pike, W. T., Christensen, U., Laudet, P., et al. (2019). SEIS: Insight's seismic experiment for internal structure of Mars. *Space Science Reviews*, *215*(1), 12. https://doi.org/10.1007/s11214-018-0574-6

Manga, M., & Wright, V. (2021). No cryosphere-confined aquifer below InSight on Mars. *Geophysical Research Letters*, *48*(8), e2021GL093127. https://doi.org/10.1029/2021gl093127

Marinova, M. M., Aharonson, O., & Asphaug, E. (2008). Mega-impact formation of the Mars hemispheric dichotomy. *Nature*, *453*(7199), 1216–1219. https://doi.org/10.1038/nature07070

McLennan, S., & Grotzinger, J. (2008). The sedimentary rock cycle of Mars. In J. Bell (Ed.), *The martian surface: Composition, mineralogy and physical properties (Cambridge planetary science)* (pp. 541–577). Cambridge University Press.

McLennan, S. M. (2012). Geochemistry of sedimentary processes on Mars. In J. P. Grotzinger & R. E. Milliken (Eds.), *Mars sedimentology* (Vol. 102, pp. 119–138). SEPM Special Publication.

McLennan, S. M., Grotzinger, J. P., Hurowitz, J. A., & Tosca, N. J. (2019). The sedimentary cycle on early Mars. *Annual Review of Earth and Planetary Sciences*, *47*(1), 91–118. https://doi.org/10.1146/annurev-earth-053018-060332

Panning, M. P., Beucler, É., Drilleau, M., Mocquet, A., Lognonné, P., & Banerdt, W. B. (2015). Verifying single-station seismic approaches using Earth-based data: Preparation for data return from the InSight mission to Mars. *Icarus*, *248*, 230–242. https://doi.org/10.1016/j.icarus.2014.10.035

Panning, M. P., Banerdt, W. B., Beghein, C., Carrasco, S., Ceylan, S., Clinton, J. F., et al. (2023). Locating the largest event observed on Mars with multi-orbit surface waves. *Geophysical Research Letters*, *50*, e2022GL101270. https://doi.org/10.1029/2022GL101270

Parro, L. M., Jiménez-Díaz, A., Mansilla, F., & Ruiz, J. (2017). Present-day heat flow models of Mars. *Scientific Reports*, *7*(1), 45629. https://doi.org/10.1038/srep45629

Posiolova, L. V., Lognonné, P., Banerdt, W. B., Clinton, J., Collins, G. S., Kawamura, T., et al. (2022). Largest recent impact craters on Mars: Orbital imaging and surface seismic co-investigation. *Science*, *378*(6618), 412–417. https://doi.org/10.1126/science.abq7704

Rudnick, R. L., & Fountain, D. M. (1995). Nature and composition of the continental crust: A lower crustal perspective. *Reviews of Geophysics*, *33*(3), 267–309. https://doi.org/10.1029/95rg01302

Schimmel, M., Stutzmann, E., Lognonné, P., Compaire, N., Davis, P., Drilleau, M., et al. (2021). Seismic noise autocorrelations on Mars. *Earth and Space Science*, *8*(6), e2021EA001755. https://doi.org/10.1029/2021ea001755

Scholz, J.-R., Widmer-Schnidrig, R., Davis, P., Lognonné, P., Pinot, B., Garcia, R. F., et al. (2020). Detection, analysis, and removal of glitches from InSight's seismic data from Mars. *Earth and Space Science*, *7*(11), e2020EA001317. https://doi.org/10.1029/2020ea001317

Smith, D. E., Zuber, M. T., Frey, H. V., Garvin, J. B., Head, J. W., Muhleman, D. O., et al. (2001). Mars Orbiter Laser Altimeter: Experiment summary after the first year of global mapping of Mars. *Journal of Geophysical Research*, *106*(E10), 23689–23722. https://doi.org/10.1029/2000je001364

Stähler, S. C., Khan, A., Banerdt, W. B., Lognonné, P., Giardini, D., Ceylan, S., et al. (2021a). *Interior models of Mars from inversion of seismic body waves (version 1.0)*. IPGP Data Center.

Stähler, S. C., Khan, A., Banerdt, W. B., Lognonné, P., Giardini, D., Ceylan, S., et al. (2021b). Seismic detection of the martian core. *Science*, *373*(6553), 443–448. https://doi.org/10.1126/science.abi7730

Stutzmann, É., Schimmel, M., Lognonné, P., Horleston, A., Ceylan, S., van Driel, M., et al. (2021). The polarization of ambient noise on Mars. *Journal of Geophysical Research: Planets*, *126*(1), e2020JE006545. https://doi.org/10.1029/2020je006545

Tanaka, K. L., Skinner, J. A., Jr., Dohm, J. M., Irwin, R. P., III, Kolb, E. J., Fortezzo, C. M., et al. (2014). Geologic map of Mars.

Taylor, S. R., & McLennan, S. M. (2009). *Planetary crusts: Their composition, origin and evolution* (p. 378). Cambridge University Press.

Thiriet, M., Michaut, C., Breuer, D., & Plesa, A.-C. (2018). Hemispheric dichotomy in lithospheric thickness on Mars caused by differences in crustal structure and composition. *Journal of Geophysical Research: Planets*, *123*(4), 823–848. https://doi.org/10.1002/2017je005431

Trampert, J., & Woodhouse, J. H. (1996). High resolution global phase velocity distributions. *Geophysical Research Letters*, *23*(1), 21–24. https://doi.org/10.1029/95gl03391

Wieczorek, M. A., Broquet, A., McLennan, S. M., Rivoldini, A., Golombek, M., Antonangeli, D., et al. (2022). InSight constraints on the global character of the Martian crust. *Journal of Geophysical Research: Planets*, *127*(5), e2022JE007298. https://doi.org/10.1029/2022je007298

Wilson, L., & Head III, J. W. (1994). Mars: Review and analysis of volcanic eruption theory and relationships to observed landforms. *Reviews of Geophysics*, *32*(3), 221–263. https://doi.org/10.1029/94rg01113

Xu, Z., Stutzmann, E., Lognonné, P., Schimmel, M., Montagner, J.-P., & Kawamura, T. (2022). Radial anisotropy from surface-wave observation in Mars. In *Europlanet science congress 2022, Granada, Spain, 18–23 September 2022, EPSC2022-863*. https://doi.org/10.5194/epsc2022-863

Zhong, S., & Zuber, M. T. (2001). Degree-1 mantle convection and the crustal dichotomy on Mars. *Earth and Planetary Science Letters*, *189*(1–2), 75–84. https://doi.org/10.1016/s0012-821x(01)00345-4

Zhou, Y., Dahlen, F. A., & Nolet, G. (2004). Three-dimensional sensitivity kernels for surface wave observables. *Geophysical Journal International*, *158*(1), 142–168. https://doi.org/10.1111/j.1365-246x.2004.02324.x

References From the Supporting Information

McSween Jr., H. Y., Taylor, G. J., & Wyatt, M. B. (2009). Elemental composition of the Martian 505 crust. *Science*, *324*(5928), 736–739. https://doi.org/10.1126/science.1165871

Toksöz, M. N., Cheng, C. H., & Timur, A. (1976). Velocities of seismic waves in porous rocks 503. *Geophysics*, *41*(4), 621–645. https://doi.org/10.1190/1.1440639